High-resolution characterization of microstructural evolution in $Rb_xFe_{2-y}Se_2$ crystals on annealing

S. C. Speller,[1,*] P. Dudin,[2] S. Fitzgerald,[1] G. M. Hughes,[1] K. Kruska,[1] T. B. Britton,[3] A. Krzton-Maziopa,[4] E. Pomjakushina,[5] K. Conder,[5] A. Barinov,[6] and C. R. M. Grovenor[1]

[1]*Department of Materials, University of Oxford, Oxford OX1 3PH, United Kingdom*
[2]*Diamond Light Source, Harwell Science and Innovation Campus, Didcot OX11 0DE, United Kingdom*
[3]*Department of Materials, Imperial College, London SW7 2AZ, United Kingdom*
[4]*Warsaw University of Technology, Faculty of Chemistry, Noakowskiego St.3, 00-664 Warsaw, Poland*
[5]*Laboratory for Developments and Methods, Paul Scherrer Institut, CH-5232 Villigen PSI, Switzerland*
[6]*Elettra-Sincrotrone Trieste ScPA, 34149 Basovizza, Trieste, Italy*

(Received 4 June 2014; revised manuscript received 27 June 2014; published 30 July 2014)

The superconducting and magnetic properties of phase-separated $A_xFe_{2-y}Se_2$ compounds are known to depend on postgrowth heat treatments and cooling profiles. This paper focuses on the evolution of microstructure on annealing and how this influences the superconducting properties of $Rb_xFe_{2-y}Se_2$ single crystals. We find that the minority phase in the as-grown crystal has increased unit cell anisotropy (c/a ratio), reduced Rb content, and increased Fe content compared to the main phase. The microstructure is rather complex, with two-phase mesoscopic plate-shaped features aligned along {113} habit planes. The minority phases are strongly faceted on the {113} planes, which we have shown to be driven by minimizing the volume strain energy introduced as a result of the phase transformation. Annealing at 488 K results in coarsening of the mesoscopic plate-shaped features and the formation of a third distinct phase. The subtle differences in structure and chemistry of the minority phase(s) in the crystals are thought to be responsible for changes in the superconducting transition temperature. In addition, scanning photoemission microscopy has clearly shown that the electronic structure of the minority phase has a higher occupied density of states of the low binding energy Fe3d orbitals, which is characteristic of crystals that exhibit superconductivity. This demonstrates a clear correlation between the Fe-vacancy-free phase with high c/a ratio and the electronic structure characteristics of the superconducting phase.

DOI: 10.1103/PhysRevB.90.024520 PACS number(s): 74.70.Xa, 74.25.Jb, 61.72.−y, 81.40.−z

I. INTRODUCTION

Binary FeSe, with a superconducting transition temperature of 8 K, is the simplest of the family of iron-based superconductors, consisting of tetrahedrally coordinated FeSe layers stacked with no spacing atoms [1]. Its transition temperature can be increased to 14 K by substitution of about half of the Se atoms with larger Te atoms [2,3]. In 2010, it was discovered that the introduction of potassium atoms between the FeSe layers in the crystal structure produced a ternary compound with nominal composition of $K_xFe_2Se_2$, and significantly increased the superconducting transition temperature to ≈30 K [4]. Subsequently, superconductivity has been found in a range of compounds in this family ($A_xFe_{2-y}Se_2$, where $A = $ K, Cs, Rb, Tl, etc.). The compositions of these compounds are well known to deviate from the ideal stoichiometry [5], with Fe vacancies introduced into the structure owing to restrictions on the valency of the iron atom. At least five different types of iron ordering have been found in $A_xFe_{2-y}Se_2$ compounds using both bulk techniques such as x-ray and neutron diffraction and high-resolution (HR) techniques such as transmission electron microscopy (TEM) and scanning tunneling microscopy (STM), as discussed in a review article by Mou *et al.* [5]. Experimentally determined phase diagrams for $Rb_xFe_{2-y}Se_2$ [6] and $K_xFe_{2-y}Se_2$ [7] indicate that antiferromagnetic (AFM) ordering occurs at temperatures above 500 K, with superconductivity coexisting with this AFM phase over a narrow range of compositions. Compounds with compositions on either side of this region are insulating (or semiconducting), exhibiting different forms of AFM ordering and vacancy ordering schemes. There is an ongoing debate about the parent compound of this system. Some suggest it is the insulating $\sqrt{5}\times\sqrt{5}$ ordered Fe-vacancy phase with composition $A_{0.8}Fe_{1.6}Se_2$ (known as the "245" phase) which exhibits block AFM ordering [6–8]. In order to obtain the superconducting phase, extra Fe must be added as Fe vacancies are considered to be detrimental to superconductivity [9,10]. Alternatively, there has been speculation that the parent compound is a semiconducting phase (based on ARPES experiments) [11] or an $\sqrt{8}\times\sqrt{10}$ ordered Fe-vacancy phase with composition $A_2Fe_7Se_8$ (based on chemical microanalysis and STM) [12].

Scanning electron microscopy (SEM) [13–15], TEM [9,16], STM [17], nanofocused x-ray diffraction (XRD) studies [18], and scanning near-field optical microscopy (SNOM) [19] have all shown that strong phase separation exists in crystals that exhibit large shielding fractions in magnetization measurements, and this two-phase nature is supported by muon-spin rotation [20,21], Mössbauer [14], x-ray and neutron diffraction [22], and NMR [10] experiments, all indicating that the volume fraction of the superconducting phase is small (≈10%), even in crystals exhibiting 100% magnetic shielding. The composition of the minority superconducting phase is still under debate. While there is consensus about the low concentration of Fe vacancies, the alkali-metal content is less clear, with NMR results reporting a composition of $Rb_{0.3}Fe_2Se_2$ [10], whereas refinement of neutron powder

*Corresponding author: susannah.speller@materials.ox.ac.uk

diffraction patterns gives $Rb_{0.6}Fe_2Se_2$ [22] and high-quality plan-view TEM/energy-dispersive x-ray (EDX) analysis on potassium compounds gives a composition of $K_{0.5}Fe_2Se_2$ [17]. It is generally believed that this minority phase is superconducting, while the majority phase is the insulating "245" vacancy ordered phase. The morphology of the minority phase in Cs compounds is shown by cross-sectional HR-SEM to consist of a three-dimensional network of interconnected plates on the mesoscale [13], which explains some of the apparently contradictory properties of these compounds, such as high T_c values and large shielding fractions coupled with large antiferromagnetic volume fractions and high normal-state electrical resistivity.

Postgrowth heat treatments have been found to strongly influence the superconductivity in $Rb_xFe_{2-y}Se_2$ crystals, with significant improvements to onset T_c and transition width achieved with annealing and quenching from modest temperatures. The cooling rate is also found to be crucial to the superconducting properties, with fast cooling from the growth temperature required to achieve high shielding fractions [15,23]. This paper addresses the effects of annealing on microstructural development in the $Rb_xFe_{2-y}Se_2$ system in order to understand the influence of microstructure on the superconducting and magnetic properties, and to enable optimization of the growth process.

II. EXPERIMENTAL METHODS

A. Samples

Single crystals of $Rb_xFe_{2-y}Se_2$ were prepared by Bridgman growth using the process described elsewhere [24]. The as-grown (AG) crystal has been cooled from 750 K by quenching at a rate of -200 K/min. The crystal was then separated into different fragments in a He glovebox and resealed under vacuum in separate quartz tubes to prevent chemical degradation. Two samples were then annealed for 3 hours at 488 K (A488) and 563 K (A563), followed by quenching. These temperatures were selected as they correspond to the phase-separation temperature and a temperature above the ordering temperature, respectively [22,25]. A wide range of superconducting and magnetic property measurements including magnetization, transport resistivity, and muon-spin rotation (μSR) have previously been reported for the same batch of crystals [25], and structural data from x-ray and neutron diffraction have also been obtained on another similar batch of AG crystals before and after annealing at 100 hours at 488 K [22]. All samples exhibited 100% magnetic shielding in magnetization measurements, and annealing at 488 K and quenching resulted in an improvement in the superconducting properties, with slightly increased T_c values (of $\approx$5%) and significantly decreased transition widths [25]. Annealing at the higher temperature of 563 K was found to be detrimental, reducing the onset T_c to about 20 K. Both μSR and neutron diffraction confirmed the presence of $\approx$10% minority (superconducting) phase in the AG crystals. The crystal structure of the minority phase is found to be compressed along the a axis and expanded along the c axis. However the μSR results indicate that the volume fraction of the superconducting (nonmagnetic) phase was unchanged upon annealing for 60 hours at 488 K, but the nonmagnetic phase is found to be distributed on a finer spatial scale after annealing. In contrast, the neutron experiments showed a decrease in the volume fraction of the minority superconducting phase for a crystal annealed at the same temperature for the longer time of 100 hours.

B. Microstructural characterization

High-resolution electron backscatter diffraction (HR-EBSD) experiments were carried out on freshly cleaved (001) surfaces in a JEOL 6500F SEM using an EDAX/TSL Digiview II detector. This technique is used to map changes in unit cell anisotropy, through cross correlation of electron diffraction patterns and subsequent analysis (described in [26]). HR-EBSD can determine relative changes in c and a values, but cannot determine absolute c and a values. Therefore, the absolute c/a values have been calculated by setting the modal c/a ratio of each map to 3.711 (based upon XRD measurements [22]). Cross-sectional imaging and serial sectioning were performed on a Zeiss NVision FIB, with AVIZO software used for three-dimensional (3D) image reconstruction. A JEOL 5510 SEM with an Oxford Instruments X-act EDX detector was used for SEM and quantitative EDX and a Zeiss Merlin SEM with a 150 mm^2 Oxford Instruments X-max detector was used for low-voltage SEM imaging and high-resolution EDX. Scanning photoemission microscopy (SPEM) was performed at the SpectroMicroscopy beam line at Elettra synchrotron [27] using a 74 eV photon light source.

III. HIGH-RESOLUTION ELECTRON BACKSCATTER DIFFRACTION ANALYSIS

Figure 1 shows typical HR-EBSD maps from AG, A488, and A563 samples. The microstructure of the AG sample [Fig. 1(a)] is very similar to the $Cs_xFe_{2-y}Se_2$ samples studied previously [13], consisting of a square network of linear features oriented along the $\langle 110 \rangle$ directions with a larger c/a ratio than the main phase (matrix). The three-dimensional morphology associated with these features can be seen from cross-sectional focused ion beam (FIB)/SEM to consist of a network of plates aligned along the {113} habit planes, as previously seen in both the Cs and K analogues [13,28]. The plates typically appear discontinuous (stripey) as more clearly seen in the 3D reconstruction of the minority phase produced by serial FIB polishing in the cross section (Fig. 2).

Annealing at the nominal phase separation temperature (488 K) results in two main changes to the microstructure: the separation of the mesoscopic plate features increases from $\approx$3 to 5–10 μm, and the c/a ratio within these features decreases to a value closer to that of the matrix. The mesoscopic features are also less regularly spaced with a larger variability in their c/a values. The EBSD pattern quality is found to be considerably poorer within the plate-shaped features, probably owing to even finer-scale phase separation (stripes) within the plates. This makes it possible to isolate the minority phase by thresholding the maps using the mean angular error (MAE) parameter from the image correlation procedure [see Figs. 1(d) and 1(e)]. While it is not possible to obtain an accurate measure of the volume fraction of the minority phase from this process, as the finer-scale phase separation is not resolved, it is clear

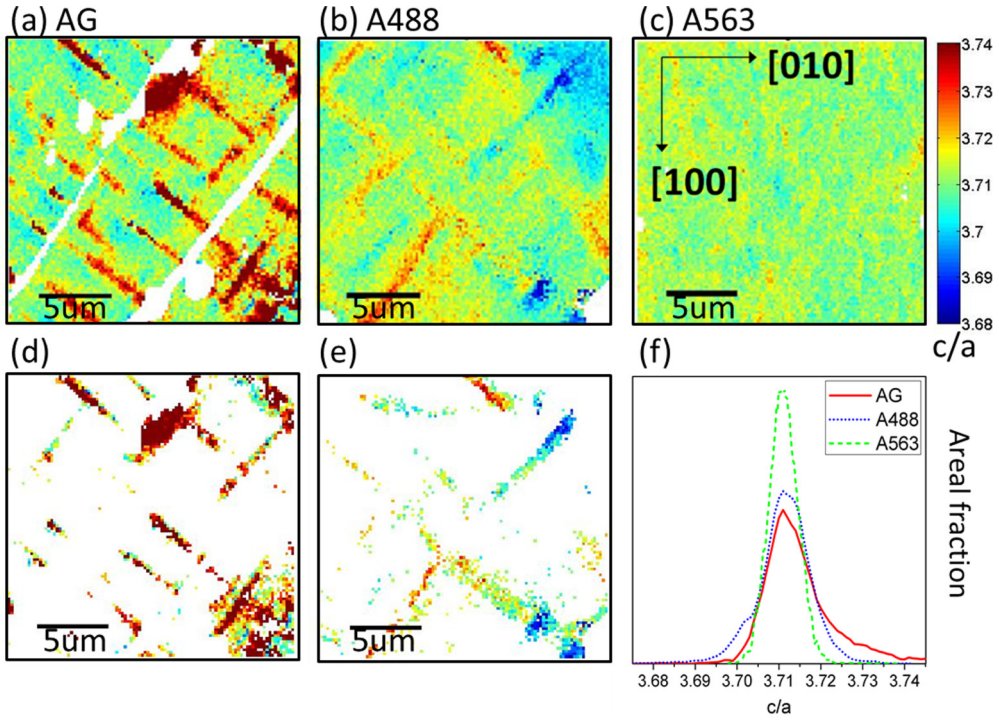

FIG. 1. (Color online) HR-EBSD maps from (a) as-grown, (b) 488 K annealed, and (c) 563 K annealed crystals showing spatial variations in the c/a ratio. HR-EBSD maps for (d) AG and (e) A488 thresholded on MAE $>$ 0.009 and MAE $>$ 0.007, respectively. (f) Probability distribution of c/a ratio for each map, with the white pixels (poor-quality data) removed.

that in the AG sample, all of the plate features have a higher c/a ratio than the matrix. However, in the sample annealed at 488 K, some of the plates have a higher c/a ratio, but others have a similar or lower c/a ratio than the matrix, suggesting the presence of at least two different additional phases. Annealing at the higher temperature of 563 K, above the Fe-vacancy ordering temperature of $\approx$541 K, produces a much more homogeneous microstructure on the length scale probed by the HR-EBSD technique ($>$100 nm) with only small fluctuations of $\Delta c/a < 0.005$ on the length scale of $\approx$1 μm and with no sign of the mesoscopic plate-shaped features seen in the AG and A488 samples. Similar fluctuations are observed in the matrix of the A488 samples and are within the noise threshold.

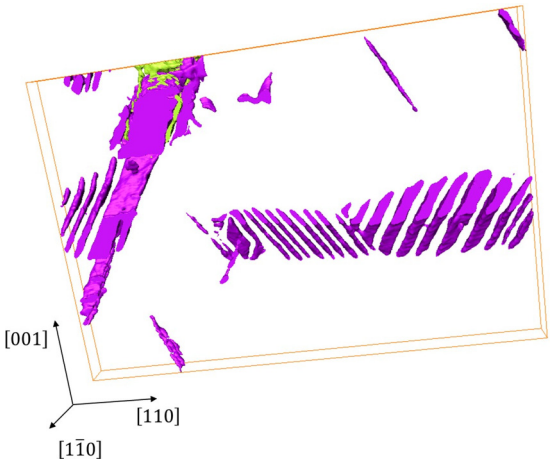

FIG. 2. (Color online) Three-dimensional reconstruction of the minority phase in the as-grown crystal produced by serial FIB sectioning. The yellow phase near the surface of the crystal is oxide which is present as the surface and was not freshly cleaved for the cross-sectional analysis. The reconstructed volume is $10\times7.5\times0.8$ μm in size.

The probability distribution of c/a values for the AG sample shows a skew towards higher c/a values with a shoulder visible on the high c/a side of the peak. This distribution has been fitted to a two Gaussian model, with the majority peak having mean $c/a = 3.711$, $\sigma = 0.0046$ and the minority peak having mean c/a=3.721, σ=0.0091. This increase in the c/a ratio in the minority phase relative to the matrix is considerably smaller than the 3.5% increase found by XRD on similar Rb crystals [22]. This is believed to be a result of the nanoscale stripey phase separation within the plate-shaped features. If the volume from which the backscattered electrons originated in the sample is bigger than the secondary phase domains, the EBSD patterns would be a superposition of the patterns for the high c/a phase with the lower c/a matrix phase, which in practice produces a smearing of the bands on the diffraction pattern, resulting in an intermediate value of c/a being measured. The Gaussian fits for the majority peaks in both the AG and A488 samples have $\frac{\text{FWHM}}{\text{average(c/a)}}$ of 0.3%, identical to the neutron-scattering data [22]. The c/a distribution of the A563 sample is well described by a single Gaussian distribution with the smaller standard deviation of 0.0035, indicating a reduction in the extent of chemical inhomogeneity and/or local mechanical strains in this sample. (See Supplemental Material for more details of the peak fitting [29]).

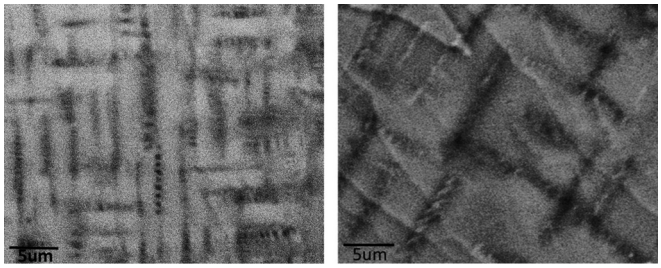

FIG. 3. 20 kV backscattered electron images showing compositional variations in AG (left panel) and A488 samples (right panel).

IV. CHEMICAL COMPOSITION ANALYSIS

The multiphase microstructures present in the AG and A488 samples have been studied further in the SEM using backscattered electron (BSE) imaging in the compositional mode and EDX microanalysis (Figs. 3 and 4). The increase in the length scale of the mesoscopic plate-shaped features on annealing is immediately apparent in Fig. 3, and thresholding the BSE image contrast using IMAGEJ software gives an areal fraction of the dark contrast phase of approximately 10% in both samples. If we correlate these plate-shaped features to the superconducting phase, this value is consistent with neutron-scattering data [22] and muon-spin rotation studies [25]. The improved spatial resolution relative to the sampling volume used in the HR-EBSD maps shows that the spacing of the fine-scale stripey phase separation within the plates also tends to increase on annealing at 488 K. In the AG sample, BSE images suggest that the mesoscopic plates consist of two phases: one with the same contrast as the matrix and the other appearing darker (lower average atomic number). Interestingly, in contrast to the AG samples, three distinct BSE contrasts can be seen in the annealed sample, suggesting the presence of two different minority phases within the matrix, one with darker BSE contrast and the other with brighter BSE contrast. Quantitative EDX at 20 kV gave majority phase compositions of $Rb_{0.81(1)}Fe_{1.55(2)}Se_2$ and $Rb_{0.81(1)}Fe_{1.58(2)}Se_2$ for the AG and A488 samples, respectively, consistent with the matrix phase being the AFM insulating "245" phase. The precise composition of the minor phases cannot be measured directly as the interaction volume at 20 kV (required to fully excite the K Se line for quantitative analysis) is significantly larger than the minority phase domains. However, since the overall composition measured over a large area of the crystal lies on a line between the matrix composition and the measured composition of the minority phase, by estimating the minority phase volume fraction of 10%, we find the actual minority phase composition to be approximately $Rb_{0.5}Fe_2Se_2$, consistent with TEM analysis for minority phases in the potassium compounds [17].

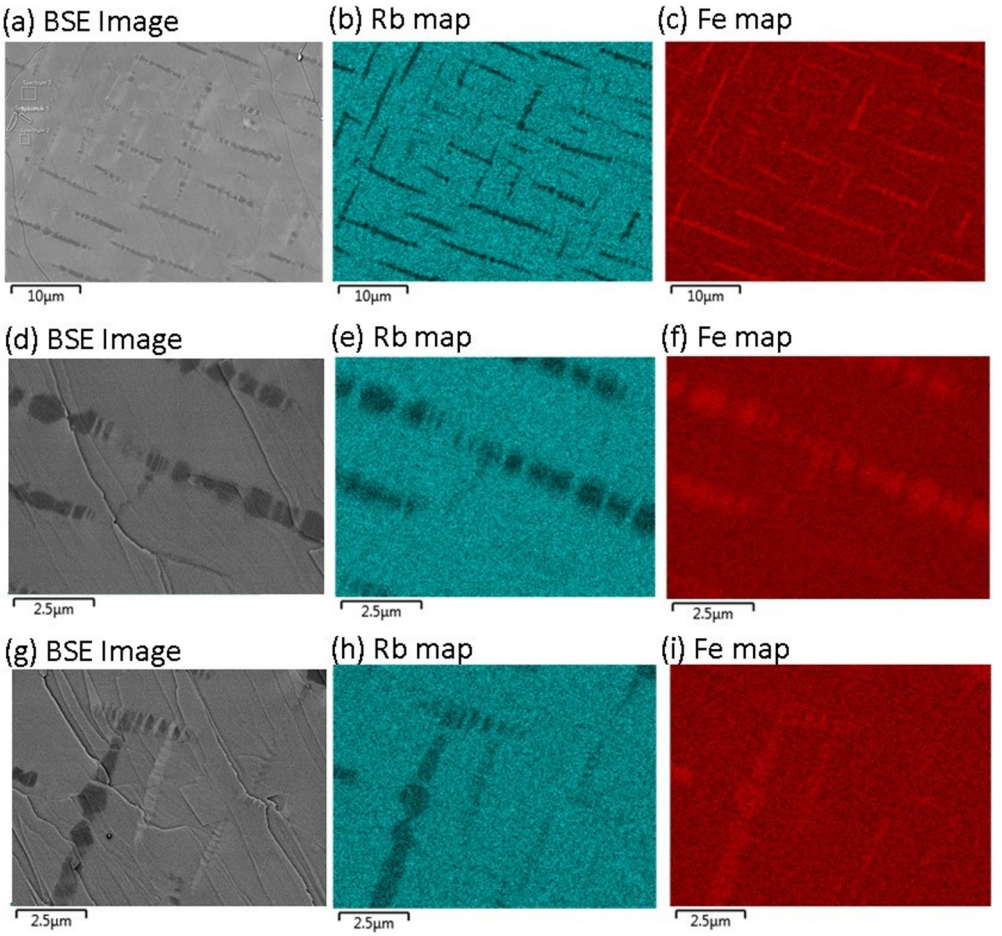

FIG. 4. (Color online) BSE images with corresponding EDX maps taken at 5 kV for three different regions of the A488 sample.

The three-phase microstructure of the 488 K annealed crystal was further investigated using 5 kV accelerating voltage to significantly reduce the EDX interaction volume. Figure 4 clearly shows that the plates with dark BSE contrast are Fe rich and Rb deficient compared to the matrix, as expected. Some of the mesoscopic plates consist of two phases, as seen in Figs. 4(d)–4(f), where one phase appears to be the same composition as the matrix and the other is the Fe-rich, Rb-deficient phase with dark BSE contrast. However, in other regions, there are some plates that have brighter contrast than the matrix and this bright phase is sometimes seen as one of the phases within stripey features, as clearly seen in Figs. 4(g)–4(i). By comparing the spectra (not shown) from the regions indicated in Fig. 4(g), it can be seen that the bright phase has an intermediate composition, i.e., still Fe rich but less Rb deficient than the dark phase. This alkali-metal partitioning on the nanoscale has also been reported recently for the K compounds and has been attributed to K ordering within one of the phases [28].

We conclude that the plate-shaped features consist of two phases in the as-grown crystal: the ordered Fe-vacancy phase with composition close to $Rb_{0.8}Fe_{1.6}Se_2$ and the "vacancy-free" superconducting $Rb_xFe_{2-y}Se_2$ phase with $y \approx 0$ and increased c/a ratio relative to the matrix. In the annealed crystals, there are at least two different minority phases present in addition to the matrix: the dark contrast vacancy-free phase (probably with increased c/a ratio) and a bright contrast phase that is also Fe rich but less Rb deficient than the dark vacancy free phase that may be the lower c/a ratio phase seen in the HR-EBSD map. It is interesting to note that high-angle annular dark-field (HAADF) scanning tunneling electron microscopy (STEM) analysis on $K_xFe_{2-y}Se_2$ crystals has also identified another phase within the Fe-rich plates which has a lower c-axis lattice parameter and contains very fine-scale low atomic number features in the (001) plane that may be cracks formed to relieve residual stress in the multiphase system. These very fine-scale features have also been observed by other researchers [19,25].

Microstructural development

In order to understand the effects of heat treatments on the superconducting and magnetic properties, it is beneficial to discuss the thermodynamic and kinetic factors affecting the complex microstructural development in this system. Previously reported differential scanning calorimetry (DSC) measurements on earlier batches of $Rb_xFe_{2-y}Se_2$ crystals [22,25] show peaks corresponding to the onset of the ordering of Fe vacancies at $T_S \approx 540$ K, the AFM Neel temperature $T_N \approx 517$ K, and a third peak attributed to the phase separation into the ordered vacancy phase plus the vacancy-free phase at $T_P \approx 488$ K. The growth process involves cooling crystals at a moderate rate from the disordered Fe-vacancy phase at high temperature. On cooling through T_S, the ordered Fe-vacancy phase forms, probably by a nucleation and growth process, rejecting excess Fe ahead of the growth interface. Wang *et al.* suggest from their *in situ* TEM studies that the Fe-vacancy ordering occurs by a spinodal mechanism, but no conclusive evidence for this has been presented. The length scale of the ordered domains is very large for spinodal microstructures, especially at low temperatures, and the interfaces between the domains appear abrupt which is more indicative of a nucleation and growth process than spinodal decomposition. The enriched Fe domains that remain between the ordered vacancy phase domains eventually decompose into two (or more) phases at T_P, producing the fine stripey appearance clearly seen in Figs. 4(d) and 4(g). It is possible that there are a number of binary eutectoid reactions in the system and slight fluctuations in the composition of the untransformed Fe-rich phase result in different volume fractions of the three phases being produced on cooling. The scale of the mesoscopic platelike microstructure is governed by the rate of diffusion that can occur below T_S during processing. The moderately fast cooling in the as-grown crystal results, as expected, in smaller scale plate separation than the samples annealed at temperatures below T_S (e.g., 488 K) in which coarsening of the mesoscopic Fe-rich plates occurs. After annealing, the quench is expected to be faster than the as-grown cooling rate, as the size of the fragments of the crystals annealed is considerably smaller than the initial crystals. This explains why the sample annealed at 563 K (above T_S) has a microstructure that is too fine to be seen in the HR-EBSD. The sample annealed at 488 K has slightly coarser phase separation within the plates than the AG sample, suggesting that the annealing temperature is slightly below T_P. However, the muon-spin rotation data on a crystal prepared under similar annealing conditions finds a reduced size of the paramagnetic (superconducting) domains. In this case, it is likely that the annealing temperature is slightly above T_P and the fine-scale microstructure is produced on quenching through T_P. Very small differences in crystal composition or furnace temperature could be responsible for the differences between the sample studied here and the one used in the muon-spin rotation experiment.

V. ELECTRONIC PROPERTIES

It remains to be explored the reason why annealing at 488 K improves T_c of the superconducting phase. One possibility is that the chemistry and resulting structural parameters of the superconducting phase change slightly as a result of the annealing and quenching procedure. This could result from local equilibration of the composition of the Fe-rich phase above T_P, a different cooling rate affecting the composition, and/or strain in the superconducting phase. Alternatively, it could be the finer scale of the phase separation within the mesoscopic plates that is responsible for the improved superconducting properties, with suggestions that superconductivity in this system is strongly influenced by the surrounding AFM matrix phase, with proximity effects enhancing T_c [30]. Therefore, the finer-scale microstructures within the plates seen in muon-spin studies on crystals annealed at 488 K [25] might be responsible for the improved properties.

To investigate the electronic properties of the different phases, scanning photoemission microscopy (SPEM) has been performed using the SpectroMicroscopy beam line at Elettra. Figure 5 compares an as-grown crystal (AG-2) with one annealed at 488 K for 3 hours (A488-2). These samples are from a different growth run than the crystals studied above, but they have been prepared under the same conditions.

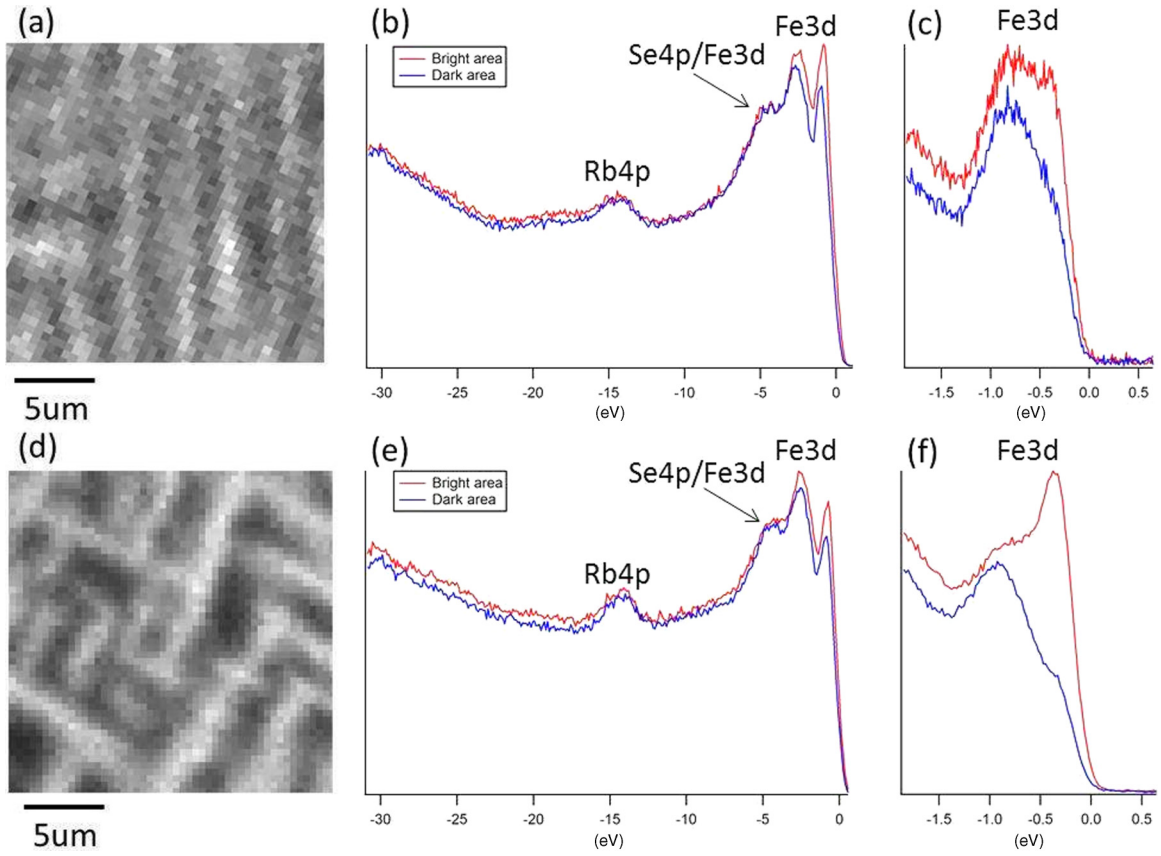

FIG. 5. (Color online) Scanning photoemission microscopy data for samples (a)–(c) AG-2 and (d)–(f) A488-2: (a), (d) near-Fermi-level maps, (b), (e) survey spectra, and (c), (f) detailed spectra near the Fermi level.

The maps in Figs. 5(a) and 5(d) show the spatial variation in the intensity of photoelectrons emitted within the energy window between 71 and 69.7 eV (corresponding to low binding energies up to −1.15 eV relative to the Fermi level at 70.85 eV) for the AG-2 and A488-2 samples, respectively. The mesoscopic platelike microstructure is clearly visible as bright features in these near-Fermi-level maps, with the scale of the microstructure being larger for the annealed sample as observed in the SEM. The lateral dimensions of these mesoscopic plate features appear to be larger in the SPEM images than in the SEM, possibly because SPEM is a much more surface-sensitive technique. The fine-scale phase separation within the plates is not typically resolved in the SPEM images, which may be a result of the inherent lower lateral spatial resolution (above 0.6 μm), or it may be an indication that the electronic structure in the matrix is modified in the vicinity of the secondary phase. The survey spectra in Figs. 5(b) and 5(e) show that the main difference between the bright and dark regions in the maps is the intensity of the lowest binding energy peaks, which are known from density functional theory (DFT) modeling to be mainly associated with Fe3d orbitals [31,32]. The more detailed valence-band spectra in Figs. 5(c) and 5(f) reveal that the low binding energy feature consists of at least two distinct peaks, with the intensity of the peak just below the Fermi level substantially higher in the plate features relative to the matrix phase. Comparing the spectra from bright regions in the AG and A488 samples shows that the increased contrast seen in the A488 image results from a significant enhancement in the lowest binding energy peak. Using classical angle-resolved photoemission spectroscopy (ARPES), Chen *et al.* found that this peak originates from the superconducting phase in $K_xFe_{2-y}Se_2$ samples [11], providing direct evidence that the bright platelike features seen in our SPEM images are the phase that becomes superconducting at lower temperatures, with the dark matrix phase having insulating properties. A simple argument based on the relative number of valence electrons per unit cell in the vacancy-ordered $Rb_{0.8}Fe_{1.6}Se_2$ phase (25.6 e per formula unit) and the vacancy-free composition $Rb_{0.5}Fe_2Se_2$ phase (28.5 e per formula unit) suggests that the higher Fe content in the vacancy-free phase leads to increased occupation of the upper Fe3d orbitals, leading to metallic/superconducting properties. More detailed analysis of the SPEM results will be the topic of a future paper.

VI. ELASTIC PROPERTIES

The {113} habit planes of the faceted minority phase domains can be understood through the stress-free transformation strain required to create them from the parent phase. Assuming a coherent interface, this is given by

$$\epsilon^{00} = \frac{F + F^T}{2} - I, \quad \text{where}$$
$$F = \begin{pmatrix} a_2/a_1 & 0 & 0 \\ 0 & a_2/a_1 & 0 \\ 0 & 0 & c_2/c_1 \end{pmatrix}, \qquad (1)$$

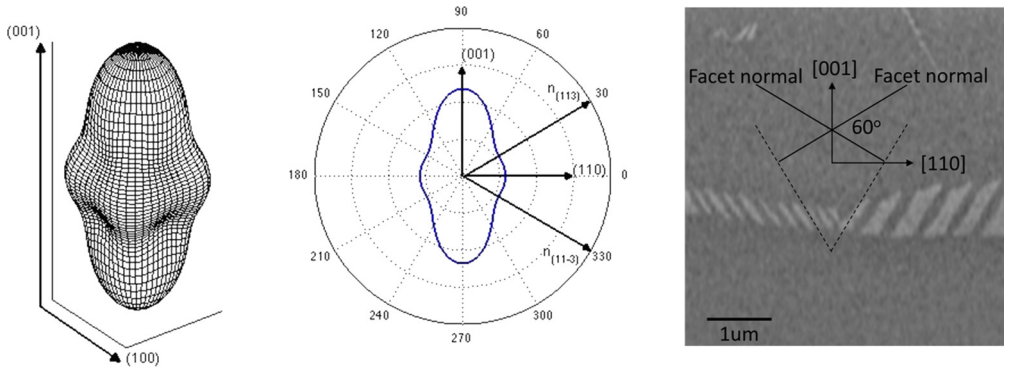

FIG. 6. (Color online) Left: Calculated energy surface as a function of facet normal n. Center: Projection onto the $(1\bar{1}0)$ plane (arb. units). Right: SEM micrograph showing the faceting in the $(1\bar{1}0)$ plane.

and a_1, c_1, a_2, c_2 are the lattice parameters of the parent and minority phases, respectively. According to the Khachaturyan-Shaltov microelasticity theory, the precipitates will form facets with normal vectors n that minimize the following energy function:

$$B(n) = \sigma^0_{ij}\epsilon^0_{ij} - n_i\sigma^0_{ij}\Omega_{jk}(n)\sigma^0_{kl}n_l, \qquad (2)$$

where $\sigma^0_{ij} = c_{ijkl}\epsilon^0_{kl}$ and $\Omega_{jk}(n) = (n_i c_{ijkl} n_l)^{-1}$ (see Shi *et al.* [33]). Taking the elastic moduli calculated for a similar compound [32], and the lattice parameters observed at the phase-separation temperature [22], gives the energy function $B(n)$ shown in Fig. 6. The left panel shows the full three-dimensional energy surface, and the center panel shows its projection onto the $(1\bar{1}0)$ plane for ease of comparison with Fig. 2. This clearly shows that the directions corresponding to the minimum B values are at an angle of 30° to the [110] direction, along the {113} plane normal directions. This explains that the faceting we observe on the {113} planes, as shown in the right panel of Fig. 6, arises as a result of minimizing the volume strain energy associated with the transformation.

VII. CONCLUSION

In conclusion, we have investigated spatial variations in crystal structure, chemistry, and electronic structure in $Rb_xFe_{2-y}Se_2$ crystals subjected to three different thermal treatments using HR-EBSD, SEM microanalysis, and SPEM. By combining our microstructural results with earlier structural and magnetic/superconducting measurements, we have developed an explanation of the phase transformations occurring in this system, which is in agreement with the physical properties. The mesoscopic plate-shaped features are believed to develop upon Fe-vacancy ordering, originating from the residual high Fe content disordered vacancy phase left between the faceted domains of the ordered phase. We have shown that the observed faceting on the {113} planes can be explained from calculations of the elastic strain energy associated with the transformation. The metastable microstructures formed during moderately fast cooling from high temperatures can be modified substantially by subsequent annealing and quenching. The HR-EBSD technique cannot image the nanoscale phase separation in these crystals, but the pattern-quality deterioration in the mesoscopic features is indicative of the presence of multiple phases at the nanoscale. The SPEM results are consistent with the minority high Fe content, high c/a phase being superconducting, and the lower c/a matrix having insulating properties. Further microstructural studies using higher spatial resolution techniques such as (S)TEM with vacuum transfer capability to avoid reaction with air are necessary for quantitative characterization of the nanoscale phase separation in these materials.

ACKNOWLEDGMENTS

S.S. was supported under the RAEng/EPSRC research fellowship scheme. A.K.-M. acknowledges the financial support founded by the National Science Centre of Poland, Grant No. DEC-2013/09/B/ST5/03391.

[1] F.-C. Hsu, J.-Y. Luo, K.-W. Yeh, T.-K. Chen, T.-W. Huang, P. M. Wu, Y.-C. Lee, Y.-L. Huang, Y.-Y. Chu, D.-C. Yan, and M.-K. Wu, PNAS **105**, 14262 (2012).
[2] M. H. Fang, H. M. Pham, B. Qian, T. J. Liu, E. K. Vehstedt, Y. Liu, L. Spinu, and Z. Q. Mao, Phys. Rev. B **78**, 224503 (2008).
[3] K. W. Yeh, Z. W. Huang, Y. L. Huang, T. K. Chen, F. C. Hsu, P. M. Wu, Y. C. Lee, Y. Y. Chu, C. L. Chen, J. Y. Luo, D. C. Yan, and M. K. Wu, Europhys. Lett. **84**, 37002 (2008).
[4] J. G. Guo, S. F. Jin, G. Wang, S. C. Wang, K. X. Zhu, T. T. Zhou, M. He, and X. L. Chen, Phys. Rev. B **82**, 180520(R) (2010).
[5] D.-X. Mou, L. Zhao, and X.-J. Zhou, Front. Phys. **6**, 410 (2011).
[6] V. Tsurkan, J. Deisenhofer, A. Günther, H.-A. Krug von Nidda, S. Widmann, and A. Loidl, Phys. Rev. B **84**, 144520 (2011).
[7] Y. J. Yan, M. Zhang, A. F. Wang, J. J. Ying, Z. Y. Li, W. Qin, X. G. Luo, J. Q. Li, J. Hu, and X. H. Chen, Sci. Rep. **2**, 212 (2012).
[8] A. E. Taylor, R. A. Ewings, T. G. Perring, J. S. White, P. Babkevich, A. Krzton-Maziopa, E. Pomjakushina, K. Conder, and A. T. Boothroyd, Phys. Rev. B **86**, 094528 (2012).

[9] W. Li, H. Ding, P. Deng, K. Chang, C. Song, K. He, L. Wang, X. Ma, J.-P. Hu, X. Chen, and Q.-K. Xue, Nat. Phys. **8**, 126 (2012).
[10] Y. Texier, J. Deisenhofer, V. Tsurkan, A. Loidl, D. S. Inosov, G. Friemel, and J. Bobroff, Phys. Rev. Lett. **108**, 237002 (2012).
[11] F. Chen, M. Xu, Q. Q. Ge, Y. Zhang, Z. R. Ye, L. X. Yang, J. Jiang, B. P. Xie, R. C. Che, M. Zhang, A. F. Wang, X. H. Chen, D. W. Shen, J. P. Hu, and D. L. Feng, Phys. Rev. X **1**, 021020 (2011).
[12] X. Ding, D. Fang, Z. Wang, H. Yang, J. Liu, Q. Deng, G. Ma, C. Meng, Y. Hu, and H.-H. Wen, Nat. Commun. **4**, 1897 (2013).
[13] S. C. Speller, T. B. Britton, G. M. Hughes, A. Krzton-Maziopa, E. Pomjakushina, K. Conder, A. T. Boothroyd, and C. R. M. Grovenor, Supercond. Sci. Technol. **25**, 084023 (2012).
[14] D. H. Ryan, W. N. Rowan-Weetaluktuk, J. M. Cadogan, R. Hu, W. E. Straszheim, S. L. Bud'ko, and P. C. Canfield, Phys. Rev. B **83**, 104526 (2011).
[15] Y. Liu, Q. Xing, K. W. Dennis, R. W. McCallum, and T. A. Lograsso, Phys. Rev. B **86**, 144507 (2012).
[16] Z. Wang, Y. J. Song, H. L. Shi, Z. W. Wang, Z. Chen, H. F. Tian, G. F. Chen, J. G. Guo, H. X. Yang, and J. Q. Li, Phys. Rev. B **83**, 140505(R) (2011).
[17] Z. A. Sun, Z. Wang, Y. Cai, Z. W. Wang, H. X. Yang, H. F. Tian, S. L. Wu, R. X. Zhang, C. Ma, B. Zhang, and J. Q. Li, Europhys. Lett. **105**, 57002 (2014).
[18] A. Ricci, N. Poccia, G. Campi, B. Joseph, G. Arrighetti, L. Barba, M. Reynolds, M. Burghammer, H. Takeya, Y. Mizuguchi, Y. Takano, M. Colapietro, N. L. Saini, and A. Bianconi, Phys. Rev. B **84**, 060511(R) (2011).
[19] A. Charnukha, A. Cvitkovic, T. Prokscha, D. Propper, N. Ocelic, A. Suter, Z. Salman, E. Morenzoni, J. Deisenhofer, V. Tsurkan, A. Loidl, B. Keimer, and A. V. Boris, Phys. Rev. Lett. **109**, 017003 (2012).
[20] Z. Shermadini, H. Luetkens, R. Khasanov, A. Krzton-Maziopa, K. Conder, E. Pomjakushina, H.-H. Klauss, and A. Amato, Phys. Rev. B **85**, 100501(R) (2012).
[21] C. N. Wang, P. Marsik, R. Schuster, A. Dubroka, M. Rossle, Ch. Niedermayer, G. D. Varma, A. F. Wang, X. H. Chen, T. Wolf, and C. Bernhard, Phys. Rev. B **85**, 214503 (2012).
[22] V. Yu. Pomjakushin, A. Krzton-Maziopa, E. V. Pomjakushina, K. Conder, D. Chernyshov, V. Svitlyk, and A. Bosak, J. Phys.: Condens. Matter **24**, 435701 (2012).
[23] Z. T. Zhang, Z. R. Yang, L. Li, Y. P. Sun, H. F. Du, L. Yang, J. Y. Pi, C. J. Zhang, M. L. Tian, and Y. H. Zhang, J. Appl. Phys. **113**, 17128 (2013).
[24] A. Krzton-Maziopa, E. Pomjakushina, and K. Conder, J. Cryst. Growth **360**, 155 (2012).
[25] S. Weyeneth, M. Bendele, F. von Rohr, P. Dluzewski, R. Puzniak, A. Krzton-Maziopa, S. Bosma, Z. Guguchia, R. Khasanov, Z. Shermadini, A. Amato, E. Pomjakushina, K. Conder, A. Schilling, and H. Keller, Phys. Rev. B **86**, 134530 (2012).
[26] S. C. Speller, T. B. Britton, G. Hughes, S. Lozano-Perez, A. T. Boothroyd, E. Pomjakushina, K. Conder, and C. R. M. Grovenor, Appl. Phys. Lett. **99**, 192504 (2011).
[27] P. Dudin, P. Lacovig, C. Fava, E. Nicolini, A. Bianco, and G. Cautero, J. Synchrotron Radiat. **17**, 445 (2010).
[28] Z. Wang, Y. Cai, Z. W. Wang, C. Ma, Z. Chen, H. X. Yang, H. F. Tian, and J. Q. Li, arXiv:1401.1001.
[29] See Supplemental Material at http://link.aps.org/supplemental/10.1103/PhysRevB.90.024520 for details of the peak fitting.
[30] S.-M. Huang, C.-Y. Mou, and T.-K. Lee, Phys. Rev. B **88**, 174510 (2013).
[31] X.-W. Yan, M. Gao, Z.-Y. Lu, and T. Xiang, Phys. Rev. B **84**, 054502 (2011).
[32] A. L. Ivanovskii, Physica C **471**, 409 (2011).
[33] R. Shi, N. Ma, and Y. Wang, Acta Mater. **60**, 4172 (2012).